MAGNETISM

Metal-organic magnets with large coercivity and ordering temperatures up to 242°C

Panagiota Perlepe[1,2], Itziar Oyarzabal[1,3]*, Aaron Mailman[4], Morgane Yquel[1,2], Mikhail Platunov[5]†, Iurii Dovgaliuk[6]‡, Mathieu Rouzières[1], Philippe Négrier[7], Denise Mondieig[7], Elizaveta A. Suturina[8], Marie-Anne Dourges[9], Sébastien Bonhommeau[9], Rebecca A. Musgrave[1], Kasper S. Pedersen[1,10], Dmitry Chernyshov[6], Fabrice Wilhelm[5], Andrei Rogalev[5], Corine Mathonière[2], Rodolphe Clérac[1]*

Magnets derived from inorganic materials (e.g., oxides, rare-earth–based, and intermetallic compounds) are key components of modern technological applications. Despite considerable success in a broad range of applications, these inorganic magnets suffer several drawbacks, including energetically expensive fabrication, limited availability of certain constituent elements, high density, and poor scope for chemical tunability. A promising design strategy for next-generation magnets relies on the versatile coordination chemistry of abundant metal ions and inexpensive organic ligands. Following this approach, we report the general, simple, and efficient synthesis of lightweight, molecule-based magnets by postsynthetic reduction of preassembled coordination networks that incorporate chromium metal ions and pyrazine building blocks. The resulting metal-organic ferrimagnets feature critical temperatures up to 242°C and a 7500-oersted room-temperature coercivity.

Magnets that operate at room temperature are usually pure metals, metal oxides, or intermetallic compounds, and they have applications in numerous aspects of our daily lives. For example, magnets are key components in data processing and storage devices, are commonly used in electrical motors that power most household appliances, and are essential in renewable energy technologies (*1*). Despite their extensive use and tremendous success in technological applications, conventional magnets present several drawbacks, such as energetically expensive fabrication (e.g., for SmCo and AlNiCo) and limited availability of key component elements (e.g., in the rare-earth–based magnets NdFeB and SmCo). Over the last three decades, various approaches have been developed to address these limitations and to target next-generation magnets. One particularly appealing strategy relies on the rational assembly of molecular building blocks, such as organic ligands and paramagnetic metal ions. These molecule-based materials exhibit behavior similar to that of traditional magnets; however, unlike the exclusively inorganic examples, they benefit from the synthetic and postsynthetic versatility that results from the molecular and coordination chemistries, which allow precise tailoring and optimization of their properties (*2*–*4*). This synthetic approach has already led to a vast number of systems with peculiar magnetic behaviors, several of which have no counterpart in inorganic materials. Among these molecule-based magnets are discrete high-spin molecules known as single-molecule magnets (SMMs) (*5*, *6*), one-dimensional (1D) magnets (single-chain magnets) (*7*), and 2D and 3D networks exhibiting magnetically ordered phases (*8*). By separating magnetic metal ions with organic ligands, these molecule-based materials feature remarkably low densities (~1 g cm^{-3}) compared with those of exclusively inorganic materials (generally >5 g cm^{-3}). Although state-of-the-art inorganic magnets are indispensable because of their high maximum energy product [i.e., high magnetic density (*9*)], complementary molecule-based magnetic materials will be of great relevance to emergent magnetoelectronic, magnetic sensing, and recording technologies as a result of their low density. However, most of these molecule-based materials suffer from low operating temperatures, which has precluded technological application.

To raise the operating temperature of molecule-based magnets, closed-shell ligands have been replaced by radicals to link paramagnetic metal ions in 2D or 3D coordination networks (*8*). The presence of a radical's spin leads to particularly strong magnetic interactions with the metal centers, which can be controlled by the chemical identity of the organic radical and metal ion, and the overlap of their magnetic orbitals containing an unpaired electron (*8*, *10*, *11*). This methodology is exemplified by the pioneering work of J. S. Miller on a family of magnets incorporating paramagnetic metal ions and organic radical species such as the tetracyanoethylene radical ($[TCNE]^{\bullet-}$) (*12*). In these systems, the strong magnetic coupling between spins localized in the metal 3d orbitals and those of the radicals result in magnetically ordered phases with critical temperatures (T_C) as high as 400 K ($V[TCNE]_x$ where $x \sim 2$) (*13*). Apart from displaying the current record T_C value measured for a molecule-based magnet, $V[TCNE]_x$ has also shed light on the applicability of molecule-based, lightweight magnets in spintronic devices, quantum information, and microwave electronics (*14*–*17*). More recently, a synthetic strategy has been developed that subjects preassembled metal-organic coordination networks to postsynthetic oxidation or reduction (acting on the ligands to form radicals or acting on the metal ions to induce mixed-valency) to obtain magnetically ordered materials at a higher temperature (maximum of 105 K until this work) than their precursors (*18*–*21*). These combined efforts have resulted in magnets with hysteresis effects on the field ($\mu_0 H$) dependence of the magnetization (M) at ambient temperature in a small number of systems, such as TCNE-based compounds and derivatives as well as several Prussian blue analogs (*2*, *3*, *12*, *22*, *23*) and covalently linked organic radical frameworks (*24*, *25*). However, all of these molecule-based magnets have failed so far to exhibit substantial room-temperature coercivity, which in the best case is on the order of hundreds of oersteds.

Herein, we report on the postsynthetic chemical reduction of two 2D coordination networks—$CrCl_2(pyz)_2$ and $Cr(OSO_2CH_3)_2(pyz)_2$ (pyz = pyrazine) (*26*, *27*)—to enhance magnetic interactions and thus increase the critical temperature of any resulting ferrimagnetic order. Although structurally similar, these two materials [$CrX_2(pyz)_2$, where X is either $[CH_3SO_3]^-$ or Cl^-] exhibit contrasting physical properties. In $Cr(OSO_2CH_3)_2(pyz)_2$, the octahedral Cr^{II} metal ions are bridged by neutral, closed-shell pyrazine ligands (pyz)^0, which transmit only weak magnetic interactions between $S = 2$ Cr^{II} spins. As a result, this material is an antiferromagnet below 10 K and an insulator (*27*). By contrast, $CrCl_2(pyz)_2$ features octahedral Cr^{III} metal ions and a mixed-valence pair of pyrazine ligands (i.e., $Cr^{III}Cl_2[(pyz)_2]^{\bullet-}$). This electronic configuration generates strong magnetic interactions between the $S = {}^3/_2$ Cr^{III} and delocalized $S = {}^1/_2$ pyrazine spins, which leads to ferrimagnetic ordering below 55 K and a substantial room-temperature electrical conductivity (*26*). In this work, we describe the postsynthetic reduction of these coordination

[1]Université de Bordeaux, CNRS, Centre de Recherche Paul Pascal, UMR 5031, F-33600 Pessac, France. [2]Université de Bordeaux, CNRS, Bordeaux INP, ICMCB, UMR 5026, F-33600 Pessac, France. [3]Chemistry Faculty, University of the Basque Country, UPV/EHU, 20018 Donostia-San Sebastián, Spain. [4]Department of Chemistry, University of Jyväskylä, FI-40014 Jyväskylä, Finland. [5]ESRF-The European Synchrotron, CS 40220, F-38043 Grenoble Cedex 9, France. [6]Swiss-Norwegian Beamlines at the European Synchrotron Radiation Facility, F-38000 Grenoble, France. [7]Université de Bordeaux, CNRS, Laboratoire Ondes et Matière d'Aquitaine, UMR 5798, F-33400 Talence, France. [8]Department of Chemistry, University of Bath, Claverton Down, Bath BA2 7AY, UK. [9]Université de Bordeaux, CNRS, Bordeaux INP, ISM, UMR 5255, F-33400 Talence, France. [10]Department of Chemistry, Technical University of Denmark, DK-2800 Kongens Lyngby, Denmark.
***Corresponding author. Email: itziar.oyarzabal@ehu.eus (I.O.); clerac@crpp-bordeaux.cnrs.fr (R.C.)**
†Present address: Kirensky Institute of Physics, Federal Research Center KSC SB RAS, 660036 Krasnoyarsk, Russia.
‡Present address: Institut des Matériaux Poreux de Paris, UMR 8004 CNRS, Ecole Normale Supérieure, Ecole Supérieure de Physique et de Chimie Industrielles de Paris, PSL Université, 75005 Paris, France.

networks, resulting in lightweight ferrimagnets with T_C up to 515 K and 7500-Oe room-temperature coercivity.

The chemical reduction of the methanesulfonate-paired 2D material was carried out through the addition of two molar equivalents of lithium 1,2–dihydroacenaphthylenide ($Li^+[C_{12}H_{10}^{\bullet-}]$; $E_{1/2}$ = −3.23 V versus $[(C_5H_5)_2Fe]^{+/o}$) (*19*) to a suspension of $Cr^{II}(OSO_2CH_3)_2(pyz)_2$ in tetrahydrofuran (THF) [Fig. 1A; see (*28*) for the detailed synthetic procedure]. A notable color change was evident upon reduction of the light brown $Cr(OSO_2CH_3)_2(pyz)_2$ to afford product **1** as an air-sensitive, dark gray, and microcrystalline powder. The powder x-ray diffraction (PXRD) pattern of **1** (fig. S1) (*28*, *29*) revealed a highly crystalline phase, with Bragg diffraction peaks corresponding exclusively to $Li[SO_3CH_3]$, which indicates that the reduced metal-organic product was either poorly crystalline, nanocrystalline, or amorphous. However, the presence of THF-insoluble $Li[SO_3CH_3]$ implied that the methanesulfonate anions were partially or fully extracted from the 2D precursor upon reduction to yield a Cr-based network possibly featuring two reduced pyrazines ($[pyz]^{\bullet-}$). X-ray absorption spectroscopy (XAS) measurements at the Cr K-edge were performed on product **1**, the $Cr(OSO_2CH_3)_2(pyz)_2$ precursor containing Cr^{II} in an octahedral coordination sphere, and a square-planar Cr^{II} reference complex $Cr(N(TMS)_2)_2(py)_2$ [noted **Cr(II)**; TMS = $Si(CH_3)_3$, py = pyridine] (*30*). The x-ray absorption near-edge structure (XANES) spectrum of **1** is markedly different from that of its precursor, as well as that of Cr oxides and Cr metal (*31*), but its features at low energy (near-edge region) and at the rising edge are notably similar to those of the square-planar **Cr(II)** reference (Fig. 1B). The near-edge structures for both product **1** and **Cr(II)**, which are the fingerprint of the Cr oxidation state in a given ligand field, show two shoulders at the same energies (~5991 and ~5994 eV). These XAS results unequivocally support that the Cr electronic structure and coordination geometry in **1** are essentially the same as in **Cr(II)**; i.e., a high-spin S = 2 Cr^{II} metal ion in a square-planar $\{Cr^{II}N_4\}$ environment (*30*). The structure of **1** is thus compatible with a 2D square coordination network, $Cr^{II}(pyz^{\bullet-})_2$, reminiscent of the precursor $Cr^{II}(pyz^{o})_2$ layer (*27*). The field dependency of the magnetization was recorded for powder **1** at various temperatures (Fig. 1C and figs. S2 to S4) (*28*), revealing broad M versus μ_0H hysteresis loops (μ_0H_{coer} = 3400 Oe at 300 K) up to at least 400 K [the temperature limit of the magnetic properties measurement system (MPMS)]. This notable magnetic behavior is in sharp contrast to that reported for any known chromium-based materials (e.g., metal, nanoparticles, or oxides; table S1) (*32*–*38*).

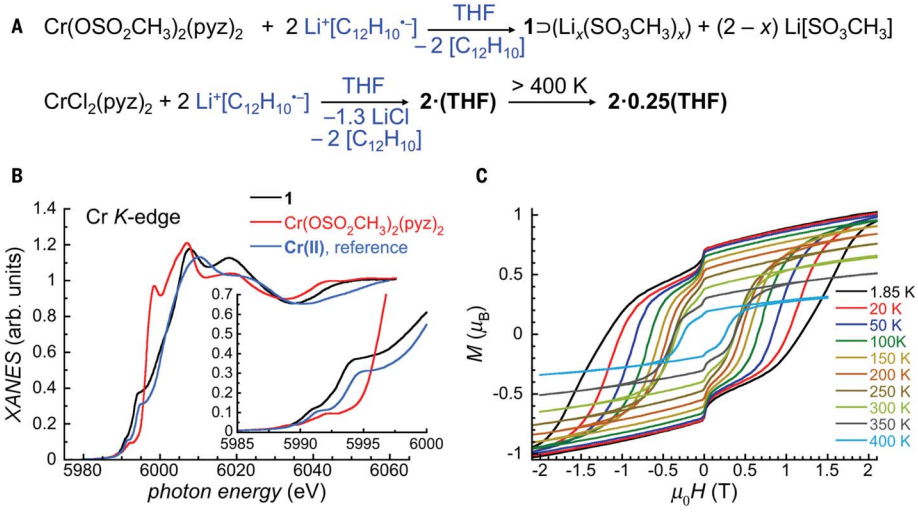

Fig. 1. Chemical reduction of $Cr(OSO_2CH_3)_2(pyz)_2$ and $CrCl_2(pyz)_2$. (**A**) Reaction schemes [solvents and soluble species in blue; solid materials in black; the ⊃ symbol indicates the presence of $Li_x(SO_3CH_3)_x$ within **1**]. (**B**) Normalized XANES spectra at the Cr K-edge region of **1** (black trace), $Cr(OSO_2CH_3)_2(pyz)_2$ (red trace), and **Cr(II)** reference (blue trace) at 295 K. Inset shows a magnified view of the near-edge region. (**C**) Magnetization versus applied *dc* magnetic field data (at 7 Oe s^{-1}) in the −2.1 to 2.1 T field range for **1** between 1.85 and 400 K. As the exact composition of **1** is unknown, the magnetization data were normalized using the molecular weight of the $Cr(OSO_2CH_3)_2(pyz)_2$ parent compound.

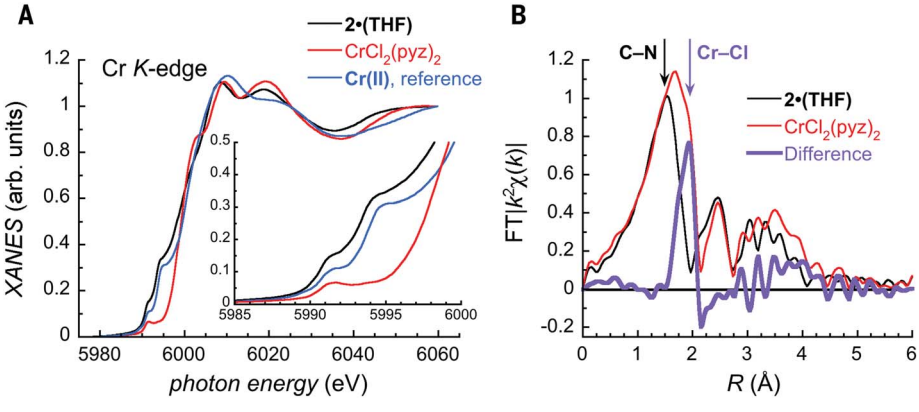

Fig. 2. XANES and EXAFS spectra at the Cr K-edge at 295 K. (**A**) Normalized XANES spectra of **2·(THF)** (black trace), $CrCl_2(pyz)_2$ (red trace), and **Cr(II)** reference (blue trace). Inset shows a magnified view of the near-edge region. (**B**) Fourier-transform (FT) EXAFS spectra for **2·(THF)** (black trace) and $CrCl_2(pyz)_2$ (red trace) (see figs. S9 and S10 for additional EXAFS data) (*28*). The difference between the two datasets is shown in purple.

The above experimental evidence unequivocally confirms that the postsynthetic chemical reduction of $Cr^{II}(OSO_2CH_3)_2(pyz)_2$ resulted in a mixture of insoluble crystalline $Li[SO_3CH_3]$ and an amorphous $Cr^{II}(pyz^{\bullet-})_2$ phase, which displayed hard magnet properties (μ_0H_{coer} = 3400 Oe at 300 K) and a critical temperature above 400 K. To target a pure analog of this room-temperature magnet, our focus turned to the related $CrCl_2(pyz)_2$ system, which is expected to yield the same magnetic material upon reduction of both the pyrazine scaffold $[[(pyz)_2]^{\bullet-} \rightarrow (pyz^{\bullet-})_2]$ and the Cr^{III} metal ion ($Cr^{III} \rightarrow Cr^{II}$). Notably, the anticipated byproduct of this reaction, LiCl (Fig. 1A), should be far easier to remove from the Cr-based product than $Li[SO_3CH_3]$ because of its increased solubility in organic media, particularly THF. Using identical experimental conditions to those for the synthesis of **1**, the $CrCl_2(pyz)_2$ precursor was exposed to $Li^+[C_{12}H_{10}^{\bullet-}]$ (Fig. 1A) (*28*). Synchrotron PXRD experiments on the resulting dark gray solid (90% isolated yield) revealed several prominent diffraction peaks and, notably, the absence of an independent crystalline LiCl phase (fig. S5) (*28*). The diffractogram was refined in the orthorhombic *Pmmm* space group with the following cell parameters: a = 6.9239(9), b = 6.9524(2), and c = 8.478(2) Å [V = 408.1(1) $Å^3$; the number between parentheses is the estimated standard deviation]. It is worth noting that the a and b

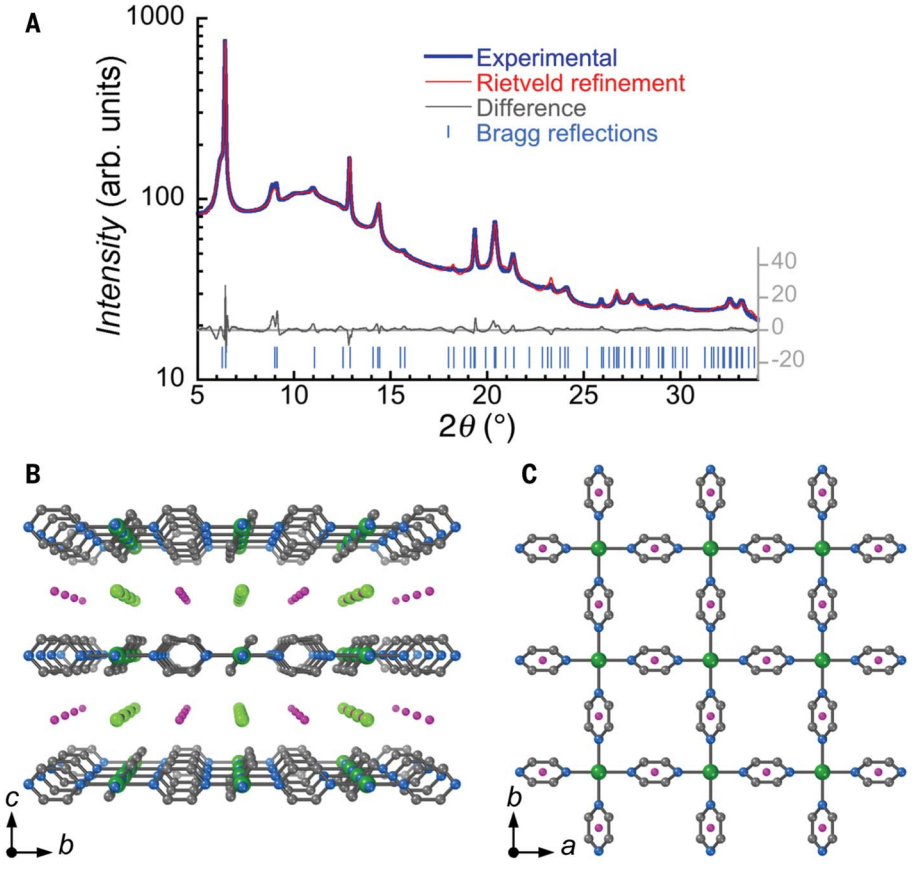

Fig. 3. Structural model of $Li_{0.7}[Cr(pyz)_2]Cl_{0.7}$·0.25(THF) [2·0.25(THF)]. (**A**) The best Rietveld refinement (red trace; R_I = 4.23%) of the synchrotron PXRD pattern of **2·0.25(THF)** at 290 K (after cooling from 500 K in a sealed capillary; blue trace) is shown with the experimental-model difference (gray trace) and calculated Bragg reflections (blue bars). (**B**) Perspective view (along the *a* direction) of **2·0.25(THF)** showing the alternation of $Li_{0.7}Cl_{0.7}$ and neutral $Cr^{II}(pyz^{\bullet-})_2$ layers stacking along the *c* direction. (**C**) Eclipsed layered structure viewed along the *c* direction. Cr is shown in dark green, N in blue, and C in dark gray. Cl (light green) and Li (pink) are shown at a fixed occupancy of 70% according to the elemental composition. Hydrogen atoms have been omitted for clarity.

lattice parameters obtained for this material [referred to as **2·(THF)** herein] are close to those found in the $CrCl_2(pyz)_2$ precursor [*Immm* space group: a = 6.90351(4), b = 6.97713(4), and c = 10.82548(6) Å; V = 521.427(6) Å^3; ρ = 1.803 g cm^{-3}]. This suggests the presence of a similar 2D $Cr(pyz)_2$-type network in both $CrCl_2(pyz)_2$ and **2·(THF)**.

The Cr K-edge XANES spectra of **2·(THF)** is remarkably similar to that of both the model square-planar complex **Cr(II)** and **1** (Fig. 1B), whereas it is clearly different from that of the precursor $Cr^{III}Cl_2(pyz)_2$ (Fig. 2A). Therefore, we conclude that the reduction of $CrCl_2(pyz)_2$ results in the reduction of octahedral high-spin Cr^{III} metal ions into square-planar high-spin Cr^{II} sites, which implies the loss of both axial chloride ligands in **2·(THF)**. Raman spectroscopy further supports this conclusion, as evidenced by the absence of the characteristic Cr–Cl symmetric stretching band (~260 cm^{-1}), whereas the position and narrow nature of Raman bands in the pyrazine fingerprint region of the spectrum (600 to 1700 cm^{-1}) suggest the presence of only reduced $[pyz]^{\bullet-}$ ligands (figs. S6 and S7 and tables S2 to S4) (*28*). To understand the reduction mechanism and the concomitant chloride decoordination, quantum chemical geometry optimizations were performed on $[CrCl_x(pyz)_4]^{2-x-q}$ molecular fragments (where the number of chloride ligands, x = 2, 1, or 0; and successive reductions are represented by q = 0, 1, 2, 3, or 4; table S5) (*28*). Upon the addition of four electrons to the initial $[CrCl_2(pyz)_4]^0$ fragment, the calculations show a minimum energy at infinite Cr···Cl distance, which indicates the instability of the fully reduced bis-chloride-bound fragment, $[CrCl_2(pyz)_4]^{4-}$. Upon the removal of chloride anions, the ability of the $[CrCl(pyz)_4]^+$ and $[Cr(pyz)_4]^{2+}$ fragments to stabilize reduced pyrazine ligands increases around the Cr^{II} center (fig. S8) (*28*). The pyrazine reduction is thus facilitated by the chloride dissociation. Moreover, the optimized structure of the $[Cr(pyz)_4]^{2-}$ fragment (q = 4, pyrazines are all reduced around the Cr^{II} center) adopts a perfect square-planar geometry (table S5) (*28*), which makes this moiety ideal for forming extended $Cr(pyz)_2$-type sheets.

A comparison of the extended x-ray absorption fine structure (EXAFS) at the Cr K-edge of **2·(THF)** and its precursor provides further experimental evidence for chloride decoordination. As shown in Fig. 2B, the Fourier-transform EXAFS spectra of $CrCl_2(pyz)_2$ and **2·(THF)** are similar except at R ~ 1.9 Å, where a marked difference is evident (see figs. S9 and S10 for EXAFS and k^2-weighted EXAFS spectra) (*28*). This corresponds to a major modification in the local environment of the Cr^{II} site. In the precursor compound, $CrCl_2(pyz)_2$, the broad feature at R = 1.67 Å and the shoulder at 1.91 Å can be attributed to the Cr–N (2.003 to 2.059 Å) and Cr–Cl (2.337 Å) bonds, respectively. However, although the Cr–N bond in **2·(THF)** is found at R = 1.53 Å, the signature of the Cr–Cl bond around R ~ 1.9 Å is pronouncedly attenuated (see difference spectrum in Fig. 2B), which corroborates the loss of axial Cl^- ions and the resulting square planar geometry at the Cr center.

Combustion elemental analysis (EA) and inductively coupled plasma optical emission spectroscopy (ICP-OES) measurements support the above assumptions and reveal the presence of 0.7(1) Li ion and 0.99(6) THF molecule per $Cr(pyz)_2$ moiety, each assumed to reside between the $Cr^{II}(pyz^{\bullet-})_2$ layers in **2·(THF)** (table S6) (*28*). Additionally, XANES measurements at the Cl K-edge for $CrCl_2(pyz)_2$ and **2·(THF)** provide evidence for remaining chlorine anions (~0.7 per Cr) in the reduced material (fig. S11) (*28*). The near-edge feature, which corresponds to an electron excitation from the Cl 1s orbital to molecular orbitals of hybridized Cl 3p and Cr 3d orbitals (*26*), is much lower in intensity in the spectrum of **2·(THF)** versus its precursor. This feature reflects a considerable weakening of the chromium-chloride interaction and subsequent elongation of the Cr···Cl distance (i.e., decoordination from the Cr metal ion) (*39*) in **2·(THF)**, which corroborates the theoretical XANES calculations (fig. S12) (*28*) and experimental EXAFS data (Fig. 2B and figs. S9 and S10) (*28*). However, the presence of a detectable near-edge signal indicates that chloride ions are still close enough to the Cr^{II} ions to interact electronically (see a comparison with LiCl in fig. S13 in which Li^+ and Cl^- ions are ionically independent) (*28*). To summarize, **2·(THF)** is a material that has neutral 2D $Cr^{II}(pyz^{\bullet-})_2$ layers of square planar Cr^{II} metal ions and two singly reduced pyrazines, separated by one THF molecule and 0.7(1) equivalents of Li^+ and Cl^- ions. The chemical formula of **2·(THF)** can therefore be defined as $Li_{0.7}[Cr(pyz)_2]Cl_{0.7}$·(THF), with a calculated density of 1.278 g cm^{-3}.

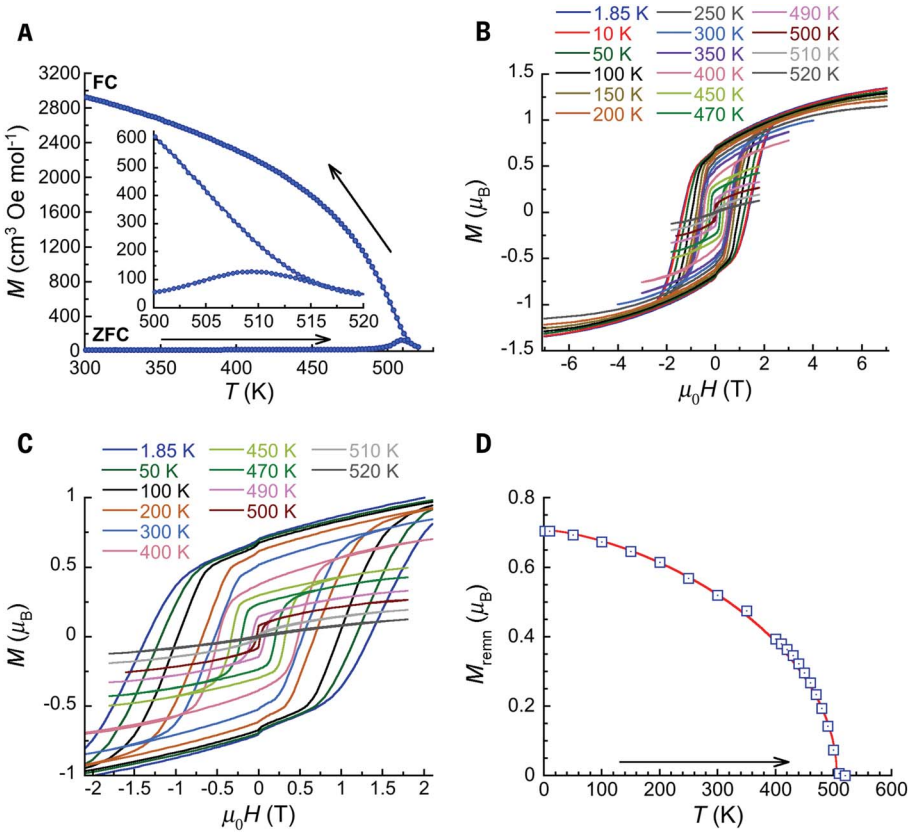

Fig. 4. Magnetic properties of 2·(THF) and 2·0.25(THF) (after partial desolvation above 400 K). (**A**) Zero field-cooled (ZFC) and field-cooled (FC) magnetization data obtained under an applied *dc* magnetic field of 50 Oe at 5 K min^{-1}. Inset shows a magnified view of the main plot in the 500 to 520 K temperature range. The solid lines are a guide for the eye. (**B**) Magnetization versus applied *dc* magnetic field data (at 5 to 12 Oe s^{-1}) in the −7 to 7 T field range, from 1.85 to 520 K (*42*). (**C**) Magnified view of selected data from (B) in the −2.1 to 2.1 T field range (*42*). (**D**) Temperature dependence of the remnant magnetization, M_{remn}, determined from the *M* versus $\mu_0 H$ data between 1.85 and 520 K [(B) and (C)]. The solid red line is the best fit to the mean-field (MF) Bloch law: $M_{remn} \propto [1 - (T/T_{C\text{-}MF})^{3/2}]^{1/2}$ with $T_{C\text{-}MF}$ = 506 K (considering data up to 490 K, χ^2(GoF) = 0.00057) (*43*).

Variable-temperature PXRD measurements on **2·(THF)** revealed an irreversible phase transformation upon heating above 380 K (fig. S14) (*28*). This phase is stable up to 500 K and remains the sole phase upon cooling to room temperature. As evidenced by thermogravimetric analysis–mass spectrometry (TGA-MS) measurements (figs. S15 to S20) (*28*), this irreversible structural change is caused by a loss of the interlayer THF molecules. However, Fourier transform infrared (FTIR) spectroscopy (figs. S21 to S24) (*28*) and EA measurements on samples of **2·(THF)** after prolonged heating (18 hours at 400 K or 10 hours at 500 K) show a residual presence of ~0.25 THF per formula unit, which is in good agreement with TGA-MS measurements (fig. S17 and table S6) (*28*). XANES measurements at the Cr K-edge of this heat-treatment product, **2·0.25(THF)**, indicated no appreciable change in the Cr^{II} coordination environment upon partial THF loss (fig. S25) (*28*). On the other hand, the Cl K-edge spectrum showed an attenuation in the near-edge region versus **2·(THF)** (fig. S26) (*28*), which indicates reduced mixing between Cl 3p and Cr 3d orbitals—i.e., greater localization of Cl p orbitals. The chlorine anions are thus slightly further from the Cr ions after the partial loss of the interlayer THF molecules. The diffractogram of **2·0.25(THF)** is less affected than that of **2·(THF)** by the anisotropic broadening of the diffraction peaks systematically associated with planes that have a nonzero *l* Miller index (Fig. 3A and figs. S14 and S27) (*28*). For both compounds, this observation implies less crystallographic order along the *c* direction (and thus in the spacing between the sheets) than within the *ab* plane of the 2D network, as is expected for layered materials (*40*, *41*). The diffractogram of **2·0.25(THF)** at 290 K was fully indexed in the tetragonal *P*4/*mmm* space group with *a* = *b* = 6.9893(1) and *c* = 7.195(3) Å [*V* = 351.5(1) $Å^3$; ρ = 1.228 g cm^{-3}; Fig. 3A and table S7] (*28*), showing that, upon removing the THF molecules, the interlayer distance diminishes, as evidenced by the decrease of the *c* parameter from ~8.5 Å in **2·(THF)** to ~7.2 Å in **2·0.25 (THF)** [for comparison the interlayer distance in the $CrCl_2(pyz)_2$ precursor is 5.4 Å].

Considering all of the above information, an appropriate structural model was used to refine the experimental PXRD pattern obtained for **2·0.25(THF)**, which yielded reasonable agreement factors (e.g., R_I = 4.23%, R_p = 1.63%, and R_{wp} = 2.32% at 290 K; Fig. 3 and table S7) (*28*). As expected, the Cr sites in **2·0.25(THF)** are bridged by pyrazine ligands forming a 2D square $Cr(pyz)_2$ network in the crystallographic *ab* plane. In contrast to the precursors $CrCl_2(pyz)_2$ and $Cr(OSO_2CH_3)_2(pyz)_2$ (*26*, *27*), these $Cr(pyz)_2$ layers in **2·0.25(THF)** are eclipsed along the *c* direction (Fig. 3C). The square-planar coordination sphere of Cr is occupied by four nitrogen atoms from four pyz ligands, with a Cr–N distance of 2.0440(6) Å. As evidenced by other techniques on **2·THF** and **2·0.25(THF)** (vide supra), the Cl^- anions are not coordinated to the Cr metal ions, but are located in between Cr sites of two adjacent layers with a Cr···Cl distance of 3.598(2) Å. In this structural model, it was not possible to localize THF molecules, but the Li cations are most likely positioned in between pyrazines for electrostatic reasons and slightly better refinement of the PXRD data.

The magnetic properties of **2·(THF)** were studied and compared with those collected for **1** (figs. S2 to S4) (*28*). Zero-field cooled (ZFC) and field-cooled (FC) magnetization data were collected under a *dc* field of 50 Oe for a sample of **2·(THF)** [and thus for **2·0.25(THF)** after partial desolvation from ~400 K onward] on a MicroSense vibrating sample magnetometer (VSM) capable of reaching temperatures up to 600 K. The magnetization bifurcation point of the ZFC and FC data, which corresponds to the temperature at which the coercive field vanishes, is found at ~510 K (Fig. 4A). This temperature agrees well with the *M* versus $\mu_0 H$ curves, which show a crossover between *S*-shape and linear (typical of a paramagnetic state) forms between 510 and 520 K (Fig. 4, B and C). As also confirmed by the vanishing of the remnant magnetization at 510 K (Fig. 4D), the critical temperature of **2·0.25(THF)** is thus ~510 K, which exceeds the ordering temperature measured for $V[TCNE]_x$ by ~110 K (*13*). It is worth emphasizing that the linear dependence of the magnetization at 520 K after the disappearance of the *M* versus $\mu_0 H$ hysteresis loops rules out the presence of any superparamagnetic nanoparticles. On cooling from 520 K to room temperature, the *M* versus $\mu_0 H$ hysteresis loops are recovered as expected for a phase transition between paramagnetic and ferri- or ferromagnetic states. Nevertheless, the absolute value of the magnetization is systematically lower than that during

the heating process (figs. S28 and S29) (*28*), which suggests that the critical temperature of **2·0.25(THF)** is in close proximity to its decomposition temperature under the experimental conditions of the magnetic measurements (i.e., in a sealed quartz tube under inert atmosphere). Similar to the powder **1** (Fig. 1C and figs. S2 to S4) (*28*), **2·(THF)** is a hard magnet with a remarkably large coercive field of 5300 Oe at room temperature (13500 Oe at 1.85 K; Fig. 4, B and C, and fig. S30) (*28*). This value compares well with those of widely used inorganic magnets and is larger than any of those observed for molecule-based magnets (which are on the order of hundreds of oersteds in the best cases; table S8) (*28*). The coercive field reproducibly displays an anomalous increase at ~350 K on the initial heating of **2·(THF)** (fig. S30) (*28*) and **1** (fig. S4) (*28*) samples, whereas no such feature is observed in the remnant magnetization, shown in Fig. 4D and figs. S29 and S3 (*28*). This anomaly of the coercive field, which is absent in measurements on **2·0.25(THF)** [prepared by annealing **2·(THF)**; figs. S30 to S35] (*28*), is thus likely linked to the partial loss of interlayer THF between ~300 and 400 K (vide supra) and the associated irreversible structural rearrangement (fig. S14) (*28*). The magnetic properties (magnetization and x-ray spectroscopy measurements; figs. S36 and S37) of **2·(THF)** and **2·0.25(THF)** samples are similar, with only slight variation in T_C (510 versus 515 K, respectively), but there is a noticeable 50% difference in the coercivity at 300 K (5300 versus 7500 Oe, respectively; Fig. 4C and figs. S32 and S37) (*28*). These results show that the annealing of **2·(THF)** to remove most of the THF molecules improves the T_C and $\mu_0 H_{coer}$ characteristics of the resulting magnet, **2·0.25(THF)**.

At 1.85 K, the magnetization of both **2·(THF)** and **2·0.25(THF)** does not saturate at 7 T, but reproducibly reaches a maximum value of 1.34 μ_B (Fig. 4B and fig. S31) (*28*). This value is systematically lower than that of 2 μ_B predicted for an ordered ferrimagnetic state with antiferromagnetically coupled spins (one $S = 2$ Cr^{II} center and two $S = ½$ pyrazine radicals; assuming g factors of 2). In an analogous manner to $CrCl_2(pyz)_2$ (*26*), the low magnetization may originate from the high degree of conjugation between the Cr d orbitals and pyrazine π orbitals, which leads to a partial delocalization of the Cr spin density over the organic scaffold and strong Cr-radical antiferromagnetic interactions. As evidenced by single-point broken-symmetry calculations performed on a $[Cr(pyz)_4]^{2-}$ fragment taken from the **2·0.25(THF)** structural model (Fig. 3, B and C), the Cr-radical exchange coupling is strongly antiferromagnetic and ranges from −336 to −427 cm^{-1} (−483 to −614 K with the $-2J$ convention) depending on the tilting of the radical pyrazines (tables S9 and S10 and figs. S38 and S39) (*28*). These strong antiferromagnetic interactions are in agreement with the ferrimagnetic order experimentally observed at high temperature for these materials.

This work reports molecule-based metal-organic magnets with high critical temperatures up to 515 K and large, room-temperature coercivity, which compete well with the characteristics of the traditional inorganic magnets and surpass the properties of previously known molecule-based magnets (table S8) (*28*). We demonstrate here that the postsynthetic chemical reduction of coordination networks is a general, simple, and efficient synthetic approach that offers broad perspectives for the preparation of a new generation of high-temperature, lightweight magnets, with yet unrealized application in emergent technologies. Finally, it should be highlighted that the reduced materials reported in this study are electrically insulating (as expected because of the absence of mixed-valency), whereas the mixed-valence $[Cr^{III}Cl_2(pyz_2)^{\bullet -}]$ precursor shows a substantial room-temperature conductivity of 32 mS cm^{-1} (*26*). Therefore, notable potential exists in fine-tuning the postsynthetic reduction of these metal-organic materials, which will lead to the further development of new high-T_C conducting molecule-based magnets.

REFERENCES AND NOTES

1. O. Gutfleisch *et al*., *Adv. Mater.* **23**, 821–842 (2011).
2. J. S. Miller, *Mater. Today* **17**, 224–235 (2014).
3. J. S. Miller, *Chem. Soc. Rev.* **40**, 3266–3296 (2011).
4. O. Kahn, *Molecular Magnetism* (VCH-Verlag, 1993).
5. D. Gatteschi, R. Sessoli, J. Villain, *Molecular Nanomagnets* (Oxford Univ. Press, 2006).
6. S. Demir, I.-R. Jeon, J. R. Long, T. D. Harris, *Coord. Chem. Rev.* **289-290**, 149–176 (2015).
7. C. Coulon, V. Pianet, M. Urdampilleta, R. Clérac, in *Molecular Nanomagnets and Related Phenomena*, S. Gao Ed. (Springer, 2014), pp. 143–184.
8. A. E. Thorarinsdottir, T. D. Harris, *Chem. Rev.* **120**, 8716–8789 (2020).
9. J. M. D. Coey, *Magnetism and Magnetic Materials* (Cambridge Univ. Press, 2010).
10. N. Motokawa, H. Miyasaka, M. Yamashita, K. R. Dunbar, *Angew. Chem. Int. Ed.* **47**, 7760–7763 (2008).
11. X. Ma *et al*., *Angew. Chem. Int. Ed.* **57**, 7841–7845 (2018).
12. J. S. Miller, S.-I. Ohkoshi, in *Molecular Magnetic Materials: Concepts and Applications*, B. Sieklucka, D. Pinkowicz, Eds. (Wiley-VCH, 2017), pp. 161–186.
13. J. M. Manriquez, G. T. Yee, R. S. McLean, A. J. Epstein, J. S. Miller, *Science* **252**, 1415–1417 (1991).
14. H. Liu *et al*., *Nat. Mater.* **17**, 308–312 (2018).
15. N. Zhu *et al*., *Appl. Phys. Lett.* **109**, 082402 (2016).
16. M. Chilcote *et al*., *APL Mater.* **7**, 111108 (2019).
17. A. Franson *et al*., *APL Mater.* **7**, 121113 (2019).
18. K. Taniguchi, J. Chen, Y. Sekine, H. Miyasaka, *Chem. Mater.* **29**, 10053–10059 (2017).
19. L. Liu, J. A. DeGayner, L. Sun, D. Z. Zee, T. D. Harris, *Chem. Sci.* **10**, 4652–4661 (2019).
20. J. A. DeGayner, I.-R. Jeon, L. Sun, M. Dincă, T. D. Harris, *J. Am. Chem. Soc.* **139**, 4175–4184 (2017).
21. L. E. Darago, M. L. Aubrey, C. J. Yu, M. I. Gonzalez, J. R. Long, *J. Am. Chem. Soc.* **137**, 15703–15711 (2015).
22. J. S. Miller, *Polyhedron* **28**, 1596–1605 (2009).
23. S. Ferlay, T. Mallah, R. Ouahès, P. Veillet, M. Verdaguer, *Nature* **378**, 701–703 (1995).
24. J. Mahmood *et al*., *Chem* **4**, 2357–2369 (2018).
25. H. Phan *et al*., *Chem* **5**, 1223–1234 (2019).
26. K. S. Pedersen *et al*., *Nat. Chem.* **10**, 1056–1061 (2018).
27. P. Perlepe *et al*., *Polyhedron* **153**, 248–253 (2018).
28. See the supplementary materials.
29. T. Trella, W. Frank, poster presented at the 17th Conference of the GDCh Division of Solid State Chemistry and Materials Research, Dresden, Germany, 15 to 17 September 2014.
30. Y.-F. Deng *et al*., *Chem. Commun.* **51**, 17688–17691 (2015).
31. S. Cuello *et al*., *J. Anal. At. Spectrom.* **31**, 1818–1829 (2016).
32. E. Fawcett, *Rev. Mod. Phys.* **60**, 209–283 (1988).
33. C. G. Shull, M. K. Wilkinson, *Rev. Mod. Phys.* **25**, 100–107 (1953).
34. G. E. Bacon, N. Cowlam, *J. Phys. C: Solid State Phys.* **2**, 238–251 (1969).
35. T. Furubayashi, I. Nakatani, *J. Appl. Phys.* **73**, 6412–6413 (1993).
36. W. Abdul-Razzaq, M. S. Seehra, *Phys. Status Solidi* **193**, 94–102 (2002).
37. S. Foner, *Phys. Rev.* **130**, 183–197 (1963).
38. J. M. D. Coey, M. Venkatesan, *J. Appl. Phys.* **91**, 8345–8350 (2002).
39. S. D. George, P. Brant, E. I. Solomon, *J. Am. Chem. Soc.* **127**, 667–674 (2005).
40. A. B. Cairns, A. L. Goodwin, *Chem. Soc. Rev.* **42**, 4881–4893 (2013).
41. T. N. Ramesh, R. S. Jayashree, P. V. Kamath, *Clays Clay Miner.* **51**, 570–576 (2003).
42. P. Perlepe *et al*., Magnetization versus applied dc magnetic field data for $Li_{0.7}[Cr(pyz)_2]Cl_{0.7}$·(THF), version 1, Zenodo (2020).
43. R. Skomski, in *Novel Functional Magnetic Materials*, A. Zhukov Ed. (Springer Series in Materials Science, Springer, 2016), pp. 359–395.

ACKNOWLEDGMENTS

The authors thank the GdR MCM-2 (Magnétisme et Commutation Moléculaires) and the MOLSPIN COST action CA15128. A. Väisänen (JYU, Jyväskylä, Finland), E. Hautakangas (JYU, Jyväskylä, Finland), P. Voisin (ESRF, Grenoble, France), J. M. Seco (UPV/EHU, Donostia-San Sebastián, Spain), G. Le Bourdon (ISM, Talence, France), L. Vellutini (ISM, Talence, France), L. Voigt (DTU, Lyngby, Denmark), Y.-G. Li (Northeast Normal University, Changchun, China; who we thank for the hydrothermal reactors), P. Dechambenoit (CRPP, Pessac, France), X. Ma (CRPP, Pessac, France), and S. De (CRPP, Pessac, France) are thanked for helpful discussions, comments, and experimental assistance. We would like to dedicate this paper to the loving memory of our colleague Dr. Ángela Valentín Pérez. **Funding:** This work was supported by the University of Bordeaux, the Région Nouvelle Aquitaine, Quantum Matter Bordeaux, and the Centre National de la Recherche Scientifique (CNRS). I.O. and R.C. are grateful to the Basque Government for I.O.'s postdoctoral grant. K.S.P. thanks the VILLUM FONDEN for a Villum Young Investigator grant (15374). A.M. thanks JYU and the Academy of Finland (project 289172) for support. **Author contributions:** R.C. conceived the original idea and formulated the research aims. P.P. executed the syntheses. A.R., F.W., M.P., P.P., I.O., M.Y., R.C., and C.M. performed the x-ray absorption spectroscopy experiments and analyzed the results. Crystallographic work was carried out by I.D., D.C., P.N., and D.M. Raman and infrared spectra were collected by S.B., A.M., I.O., and M.Y. Elemental analyses and inductively coupled plasma measurements were carried out by A.M., K.S.P., and P.P. Thermogravimetric analysis–mass spectrometry data were collected and analyzed by M.-A.D., P.P., and I.O. Magnetic measurements were conducted by P.P., M.R., R.C., and C.M. E.A.S. performed the density functional theory studies. After a first complete draft of the manuscript was written by I.O., P.P., R.A.M., C.M., and R.C., all authors were involved in finalizing the manuscript and gave their consent to its publication. **Competing interests:** The authors declare no competing interests. **Data and materials availability:** Crystallographic data of $Li_{0.7}[Cr(pyrazine)_2]Cl_{0.7}$•0.25(THF) [**2·0.25(THF)**] at 290 and 500 K are available free of charge from the Cambridge Crystallographic Data Centre under reference numbers 1983877 and 2007863, respectively. The M versus $\mu_0 H$ data shown in Fig. 4, B and C, are publicly available on Zenodo (*42*). All other data are in the main text or the supplementary materials.

SUPPLEMENTARY MATERIALS

science.sciencemag.org/content/370/6516/587/suppl/DC1
Materials and Methods
Figs. S1 to S39
Tables S1 to S10
References (*44*–*76*)

26 June 2020; accepted 11 September 2020
10.1126/science.abb3861

Metal-organic magnets with large coercivity and ordering temperatures up to 242°C

Panagiota Perlepe, Itziar Oyarzabal, Aaron Mailman, Morgane Yquel, Mikhail Platunov, Iurii Dovgaliuk, Mathieu Rouzières, Philippe Négrier, Denise Mondieig, Elizaveta A. Suturina, Marie-Anne Dourges, Sébastien Bonhommeau, Rebecca A. Musgrave, Kasper S. Pedersen, Dmitry Chernyshov, Fabrice Wilhelm, Andrei Rogalev, Corine Mathonière and Rodolphe Clérac

Science **370** (6516), 587-592.
DOI: 10.1126/science.abb3861

Lightening the load

Permanent magnets are generally produced from solid metals or alloys. Less dense compositions involving lighter elements tend to demagnetize well below room temperature or under modest applied external fields. Perlepe *et al.* now report that chemical reduction of a low-density chromium-pyrazine network produces a magnet that remains stable above 200°C and resists demagnetization with 7500-oersted coercivity at room temperature. The straightforward synthetic route to the material shows promise for broad exploration of potential applications.

Science, this issue p. 587